Journal of Applied Physics

RESEARCH ARTICLE | OCTOBER 13 2025

Magnetization-controlled terahertz harmonic generation with grating and cavity structures

Hatice Nur Koyun ; Ruslan Salikhov ; Ciaran Fowley ; Steffen Kober ; Nupur Sontakkey; Igor Ilyakov ; Thales V. A. G. de Oliveira ; Jan-Christoph Deinert ; Aleksandra Lindner ; Artur Erbe ; Jürgen Faßbender ; Manfred Helm ; Jürgen Lindner ; Stephan Winnerl ; Klaas-Jan Tielrooij ; Ryszard Narkowicz ; Sergey Kovalev

J. Appl. Phys. 138, 143907 (2025)
https://doi.org/10.1063/5.0248907

Journal of Applied Physics ARTICLE pubs.aip.org/aip/jap

Magnetization-controlled terahertz harmonic generation with grating and cavity structures

Cite as: J. Appl. Phys. 138, 143907 (2025); doi: 10.1063/5.0248907
Submitted: 10 July 2025 · Accepted: 21 September 2025 ·
Published Online: 13 October 2025

Hatice Nur Koyun,[1] Ruslan Salikhov,[1,a)] Ciaran Fowley,[1] Steffen Kober,[2] Nupur Sontakkey,[3] Igor Ilyakov,[1] Thales V. A. G. de Oliveira,[1] Jan-Christoph Deinert,[1] Aleksandra Lindner,[1] Artur Erbe,[1,4] Jürgen Faßbender,[1,5] Manfred Helm,[1,6] Jürgen Lindner,[1] Stephan Winnerl,[1] Klaas-Jan Tielrooij,[3,7] Ryszard Narkowicz,[1] and Sergey Kovalev[2,a)]

AFFILIATIONS

[1]Helmholtz-Zentrum Dresden-Rossendorf, Bautzner Landstraße 400, Dresden 01328, Germany
[2]Faculty of Physics, TU Dortmund University, Dortmund 44227, Germany
[3]Department of Applied Physics, TU Eindhoven, Eindhoven, Netherlands
[4]Institute of Semiconductors and Microsystems, TU Dresden University, Dresden 01062, Germany
[5]Institute of Solid State and Materials Physics, TU Dresden University, Dresden 01062, Germany
[6]Institute of Applied Physics, TU Dresden University, Dresden 01062, Germany
[7]Catalan Institute of Nanoscience and Nanotechnology (ICN2), BIST and CSIC, Campus UAB, Bellaterra, Barcelona, Spain

[a)]**Authors to whom correspondence should be addressed:** r.salikhov@hzdr.de and sergey.kovalev@tu-dortmund.de

ABSTRACT

Spintronic terahertz (THz) frequency conversion in ferromagnet/heavy metal (FM/HM) heterostructures has the potential to enhance high-speed data communication and advance ultrafast magnetic memory applications. By leveraging ultrafast spin currents and spin–orbit interactions in FM/HM systems, broadband THz generation can be achieved, with recent studies demonstrating spintronic THz second harmonic generation (TSHG) and optical rectification. We introduce concepts for controlling the frequency conversion and temporal characteristics of TSHG through active manipulation of FM magnetization, providing flexibility in second harmonic emission and waveform shaping. The TSHG valve is realized by employing THz metamaterials, consisting of hybrid FM/HM structures combined with subwavelength gold periodic arrays. Additionally, using microstructured gold periodic arrays, we investigate the TSHG field enhancement capability as a function of grating filling factor and explore the potential for TSHG cavity enhancement.

I. INTRODUCTION

Terahertz (THz) spintronics is an emerging research field focused on the ultrafast (on the picosecond timescale) manipulation of electron spin, aimed at enabling rapid writing, processing, and reading of magnetic states for nonvolatile memory applications.[1–4] This field promotes opto-spintronic strategies that involve converting photons into spin currents. A notable example is spintronic THz emitter (STE), where femtosecond laser pulses induce the demagnetization of a ferromagnetic (FM) layer interfaced with a heavy metal (HM). The optically induced spin-polarized electrons then propagate into the HM layer, where they are converted into charge current burst via the inverse spin Hall effect (or inverse spin Rashba–Edelstein effect), ultimately resulting in THz pulse emission.[5–8] One significant advantage of STE is its ability to control the polarization of the emitted THz pulse through the magnetization direction of the FM layer, without significant losses in emitted power.[9,10]

Besides optical excitations, THz radiation is also capable of generating spin currents in metallic FM/HM systems via the spin Hall effect (or spin Rashba–Edelstein effect), matching the efficiencies of magnetotransport experiments.[11,12] These ultrafast THz-induced spin currents can be exploited in nonlinear THz optics, such as second harmonic generation through ultrafast unidirectional spin Hall magnetoresistance[13] and third harmonic generation via spin–orbit-driven

nonlinear electron dynamics,[14] enabling THz spectroscopy to probe the spintronic properties of materials and their interfaces on picosecond timescales. Beyond the spin Hall effect, single-cycle THz pulses, much like optical pulses, can stimulate the demagnetization of ultrathin metallic FM layers.[15,16] Multi-cycle THz radiation further results in modulations of FM demagnetization, generating spin currents in the HM layer during each half-cycle of the THz pulse.[17] These modulations lead to THz second harmonic generation (TSHG) and optical rectification.[18] The microscopic origin of this spintronic frequency conversion can be understood as follows: when the THz field impinges on the FM/HM system, it causes an instantaneous increase in electron temperature at these interfaces.[16–19] This rise in electron temperature generates a spin current from the FM layer to the HM layer, which is then converted into charge currents through the inverse spin Hall (or Rashba–Edelstein) effect. Since the characteristic time of the ultrafast spin current comparable to the period of a THz wave,[16–19] the conversion of spin current to electric current, and consequently THz emission, occurs within each half-cycle of the THz excitation. These periodic modulations of spin current density, along with their conversion to charge current by the THz wave, generate second harmonic and rectification signals.[18] The spintronic TSHG conversion efficiency is comparable to that of STE and is on the order of 10^{-4} in amplitude,[18] which is significantly lower than that of currently available electronic converters. Nevertheless, the spintronic origin of this phenomenon provides an additional degree of freedom for active magnetization control over conversion efficiency, enabling on-demand tuning of TSHG emission. Furthermore, it holds the potential for rapid electrical readout of FM magnetization states by exploiting the rectified component of the TSHG.

One effective strategy to address the limitations of low power efficiency involves the implementation of subwavelength structures, such as slits, arrays of slits, or microscale resonators, to concentrate THz light within these geometries.[20–40] This field enhancement concept has been successfully realized in grating-based metamaterials, including those composed of graphene and topological insulators, thereby enabling enhanced THz harmonic generation.[38,39] Furthermore, recent research has demonstrated that the incorporation of THz cavities can improve and control THz emission from STEs.[41] In this work, we investigate microstructured periodic arrays and their field enhancement capabilities for spintronic TSHG in ultrathin FM/HM heterostructures. We also utilize these metallic periodic arrays in a cavity configuration.[41] Our observations indicate a 12-fold enhancement in TSHG intensity within the slits of the periodic arrays, suggesting an order of magnitude improvement in the efficiency of local (or near-field) TSHG sensors. Notably, we demonstrate that the intensity of TSHG can be controlled by the magnetization direction of the FM layer, resulting in TSHG signal switching. Furthermore, in the cavity configuration, we show that the magnetization can control the TSHG carrier envelope, including properties such as pulse duration and the number of cycles.

For this study, we employ grating structures with subwavelength periodicities on the order of tens of micrometers to explore the effect of them on TSHG. We design grating structures with gap sizes several orders of magnitude smaller than the 1 mm wavelength of the fundamental 0.3 THz radiation. In this scenario, the enhancement of the THz field (G) becomes independent of the fundamental radiation frequency and is given by the ratio of the grating period (P) to the gap width (w_{gap}), expressed as $G = P/w_{gap}$.[24] Additionally, such grating structures demonstrate high THz transmission, approaching unity.[24] In Sec. II, we provide experimental details on the composition of the metamaterial hybrid heterostructures, their fabrication, and characterization, including specifics about the TSHG experiment. Section III discusses the TSHG enhancement characteristics for samples with varying values of P and w_{gap}. The magnetization control of the TSHG characteristics, using grating structures in field enhancement and cavity geometries, is presented in Sec. IV. Section V offers modeling and simulations related to the experimental results, and Sec. VI concludes the paper.

II. EXPERIMENTAL DETAILS

A. Sample fabrication

To explore the field enhancement effect of microstructured periodic arrays on spintronic THz frequency conversion efficiency, we fabricated gold grating structures on Pt(2 nm)/Py(2 nm)/SiO_x(10 nm) (Py = $Ni_{81}Fe_{19}$) multilayered films, varying the grating gap size from 20 to 2 μm, as illustrated in Figs. 1(a) and 1(c). Additionally, we designed grating structures with 1 μm gap size in order to approach a higher filling factor. The Pt(2 nm)/Py(2 nm)/SiO_x(10 nm) heterostructures were fabricated at room temperature by magnetron sputtering in a 4×10^{-3} mbar Ar atmosphere in an ultrahigh-vacuum BESTEC system. The dc sputter power was set to 50 W for metallic layers, while SiO_x was deposited using rf power of 100 W. We used 1 mm-thick double-side-polished quartz (SiO_2) glass as a substrate. The thickness for all layers was controlled via the deposition time. Before the sample fabrication, the sputter rate of each material was calibrated using x-ray reflectivity characterization.

The Au grids were fabricated via standard i-line UV lithography. Samples were first cleaned in acetone with ultrasonic agitation for 5 min, then in isopropyl alcohol (IPA) for 5 min and finally rinsed under flowing de-ionized (DI) water, to ensure that the sample surface is free from contamination. Before coating with photo resist, adhesion promotor AR300-80 was applied by spin coating at 4000 rpm for 40 s followed by heat treatment on a hot plate at 100 °C for 5 min. Then, ma-N 1407 photoresist was spin coated at 4000 rpm for 40 s followed by heat treatment on a hot plate at 100 °C for 2 min. Exposure of the photoresist through the photomask containing the sample design was performed on a Karl-Süss MA6 mask aligner operated in a hard contact mode. The exposure time was 7 s. Areas of photoresist that were subjected to UV light become cross-linked and were rendered less soluble in developer. After exposure, the sample was developed in maD-533s developer for 30 s, followed by immersion in DI water which acts as a stopper for the development process. After successful lithography, a bilayer of Cr(3 nm)/Au(20 nm) is deposited using thermal evaporation for both metals, the deposition rate for Cr is ~0.2 and 0.5 nm/s for Au. Acetone and ultrasonic agitation were used for the final lift-off process. Here, acetone dissolves the remaining areas of photoresist and with it the metal bilayer resting on top. What is left behind is metal bilayer only in desired areas patterned by lithography. One sample with 20 μm stripe width and 1 μm gap was fabricated using a PMMA mask and electron beam lithography. This was due to the resolution limit of UV lithography, which is approximately 2 μm. The thickness of

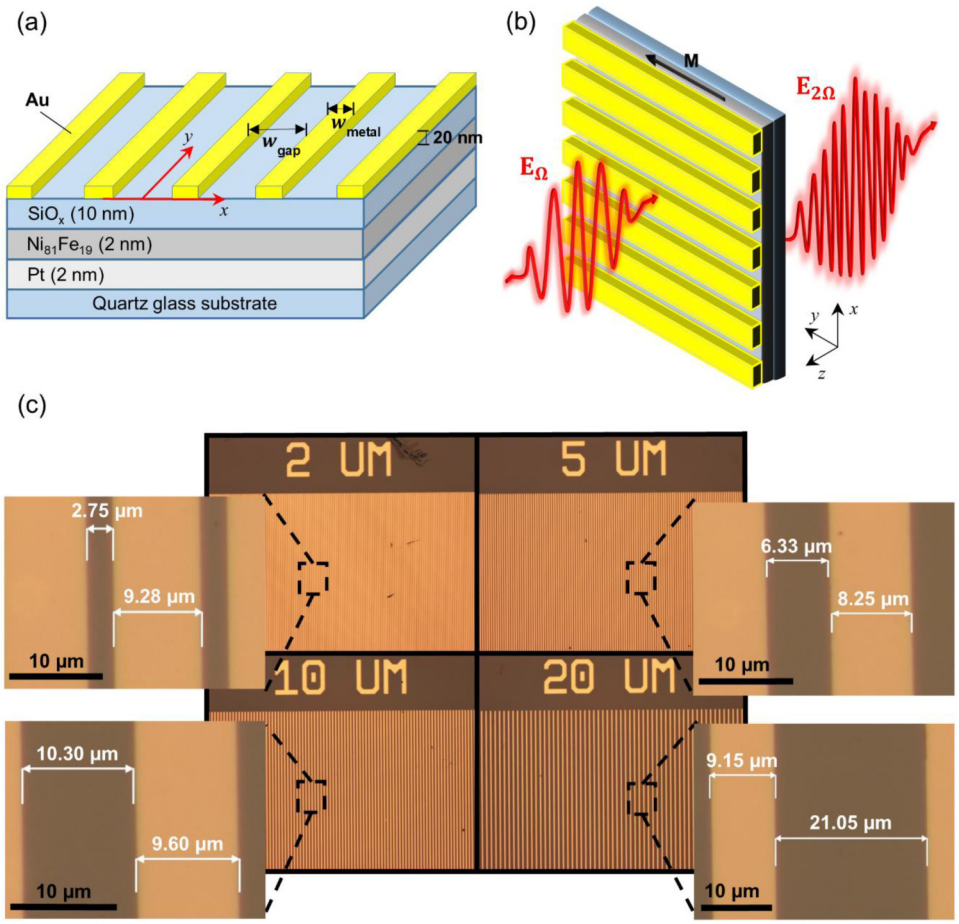

FIG. 1. (a) Schematic representation of samples designed to enhance the TSHG efficiency. The Au layers were deposited on 3 nm-thin Cr layers to enhance adhesion between Au and the SiO_x layer. (b) Schematic illustration of the geometry employed for THz time-domain spectroscopy measurements. The Py magnetization (M) was aligned parallel to the long axis of the Au bars using an external field of 100 mT. A fundamental narrowband THz pulse, E_Ω, with a frequency $\Omega = 0.3$ THz is focused onto the Au grated structure, with polarization perpendicular to the Au bar axis. (c) Optical microscope images showcasing lithographically patterned Au periodic arrays on a single 1×1 cm^2 sample, highlighting variations in the gap distances (dark contrast) between the Au bars (bright contrast).

the metal layers and the deposition technique were the same. During the sample processing, integrity of the Py/Pt heterostructure was granted by the SiO_x capping layer.

B. Time-resolved nonlinear THz spectroscopy setup

Our TSHG experimental geometry is depicted in Fig. 1(b). We utilized time-resolved THz harmonic generation spectroscopy,[38,39] employing narrowband THz pulses (E_Ω) with a central frequency of $\Omega = 0.3$ THz or $\Omega = 0.35$ THz and with a bandwidth of approximately 20%. For the laser-based (table-top) THz source, we employed a tilted pulse front generation scheme in a lithium niobate ($LiNbO_3$) crystal using 35 fs laser pulses with an 800 nm central wavelength, 1 kHz repetition rate, and 9 mJ pulse energy. We applied two 0.3 THz narrowband filters with a 20% bandwidth to convert broadband THz pulses into narrowband radiation. The resulting narrowband THz pulses were focused onto a sample with an 800 μm beam waist diameter (determined at full width at half maximum) and a peak field strength of about 100 kV/cm. The THz radiation emitted from the sample was characterized via electro-optical sampling (EOS) using a 2 mm thick ZnTe single crystal. For EOS, we used 1% of the laser pulse energy employed for THz generation. To suppress parasitic fundamental radiation at 0.3 THz, we placed additional THz bandpass filters, with high transmission at the TSHG frequency, between the sample and the EOS crystal. A permanent magnet generating an approximate magnetic field of 100 mT at the sample position was employed to align the Py magnetization direction within the sample plane and to ensure magnetic saturation of the ferromagnetic layers. The THz incident pulses (E_Ω) focused onto the sample with a metallic grating are linearly polarized along the x axis, with their electric field perpendicular to the long axis of the stripes [see Figs. 1(a) and 1(b)]. The magnetization direction of the Py layer is aligned along the y axis parallel to the long axis of the Au bars [Fig. 1(b)], causing the TSHG polarization to align collinearly with the polarization of the fundamental beam.[18] The effect of the Py magnetization direction with respect to the Au stripe long axis is discussed in Sec. IV.

III. ENHANCING FIELDS WITH GOLD GRATING

A. Gold grating transmission characteristics

First, we present the THz transmission characteristics of gold periodic arrays fabricated on quartz glass substrates [without the

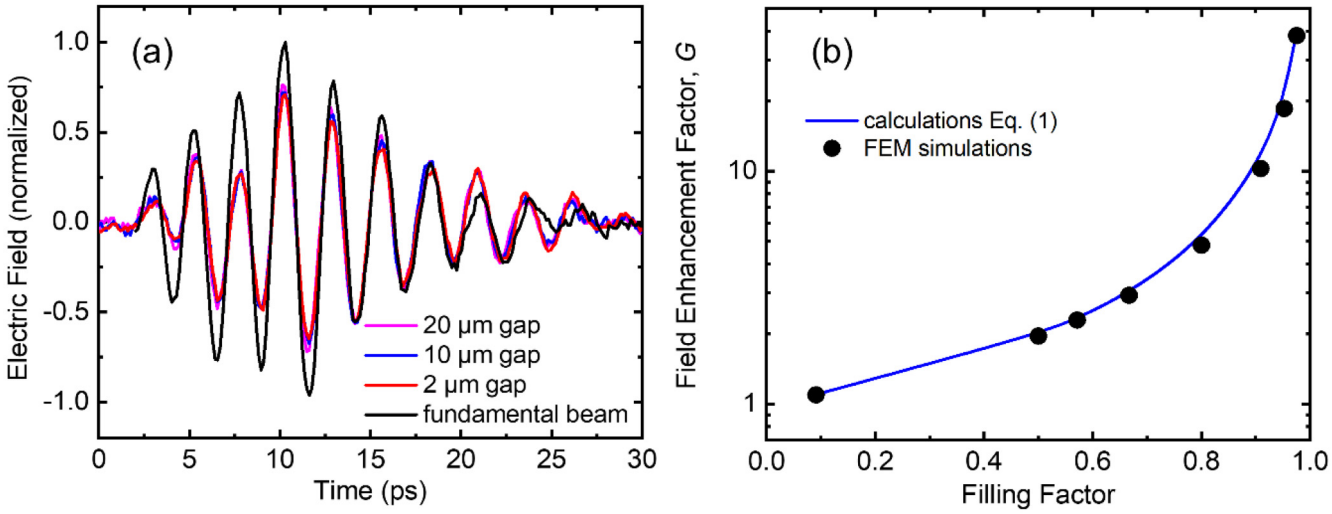

FIG. 2. (a) Transmission of fundamental pulses with a central frequency of $\Omega = 0.35$ THz through gold grating structures with varying gap sizes between 20 μm-wide Au bars. (b) Comparison of field enhancement factors as a function of Au filling factor for gold grating structures with a 20 μm Au width, calculated using analytical equation (1) (blue solid line) and obtained from FEM simulations (black circles).

Py/Pt film in Fig. 1(a)], featuring 20 nm-thick Au stripes with a width of $w_{metal} = 20\,\mu$m and variable gap widths w_{gap}. Figure 2(a) compares the direct fundamental THz pulse (E_Ω) with the transmitted pulses through gold grating structures of different gap sizes. All signals were detected using EOS, with the fundamental beam detected without any sample between the THz radiation source and the EOS crystal. Our gold grating samples exhibit reduced transmission, approximately 75% of the fundamental field amplitude, showing negligible dependence on gap width, consistent with subwavelength grating calculations previously presented in Ref. 24. This reduced transmission is attributed to the quartz glass substrate acting as a Fabry–Pérot (F–P) type resonator. This behavior is confirmed by finite element method (FEM) simulations detailed in Sec. V. The simulations (see Fig. 6) indicate oscillations in transmission power between 60% and 100%, depending on the frequency, arising from the F–P contribution.

Having experimentally confirmed that our grating structures transmit the fundamental THz field independently of the gap width, we can estimate the field enhancement factor, G, defined as the ratio of the electric field amplitude E_x averaged over the gap, to the amplitude of the incident radiation E_Ω, using the following equation from Ref. 24:

$$G = \frac{\langle E_x \rangle}{E_\Omega} = \frac{P}{w_{gap}} = \frac{1}{A_{active}} = \frac{1}{1-F}, \quad (1)$$

where A_{active} represents the relative active area, defined as $A_{active} = w_{gap}/(w_{metal} + w_{gap})$, and F is the filling factor, given by $F = w_{metal}/(w_{metal} + w_{gap})$, indicating the fraction of the total area covered by Au, hence $A_{active} = 1 - F$. Since the THz field enhancement equals to the ratio of the grating period $P = (w_{metal} + w_{gap})$ to the gap width w_{gap}, this relationship signifies that the enhancement is inversely proportional to the active area of the periodic arrays, where the field is localized between the Au stripes (i.e., within the gaps). Figure 2(b) shows the enhancement factor as a function of the Au filling factor, calculated using Eq. (1) (blue solid line). The results indicate that the average THz field amplitude within the gap increases progressively as F approaches unity. Specifically, for gap sizes ranging from 20 to 2 μm—corresponding to filling factors between 0.5 and 0.91—the THz field enhancement factor increases from nearly 2 to approximately 10. The validity of this scaling with the filling factor is further confirmed by our FEM simulations [black circles in Fig. 2(b)], demonstrating good agreement between the simulation data points and the estimation based on Eq. (1). Considering the quadratic relationship between the TSHG amplitude and the fundamental radiation,[18] this implies a potential 100-fold enhancement in TSHG amplitude conversion for the periodic array at a 2 μm gap width. However, below, we demonstrate that achieving such high TSHG conversion efficiency is hindered by the highly reflective Py/Pt metallic layer, which leads to an overall increase in reflection.

B. Gold grating TSHG intensity enhancement

Figure 3(a) shows the transmission behavior of the fundamental THz pulse (E_Ω) through a hybrid heterostructure. This structure consists of a grating similar to that used in Fig. 2(a), but it is now fabricated on a Pt(2 nm)/Py(2 nm)/SiOx(10 nm) multilayer. The pronounced dependence of THz transmission on gap size is evident. At the nominal gap size of 20 μm, the peak amplitude of the transmitted signal is approximately 75% of the radiation transmitted through the bare reference Py/Pt sample, whereas at a nominal gap size of 2 μm, the transmission decreases to 45%. This result stems from the increased overall THz reflection in the active area between

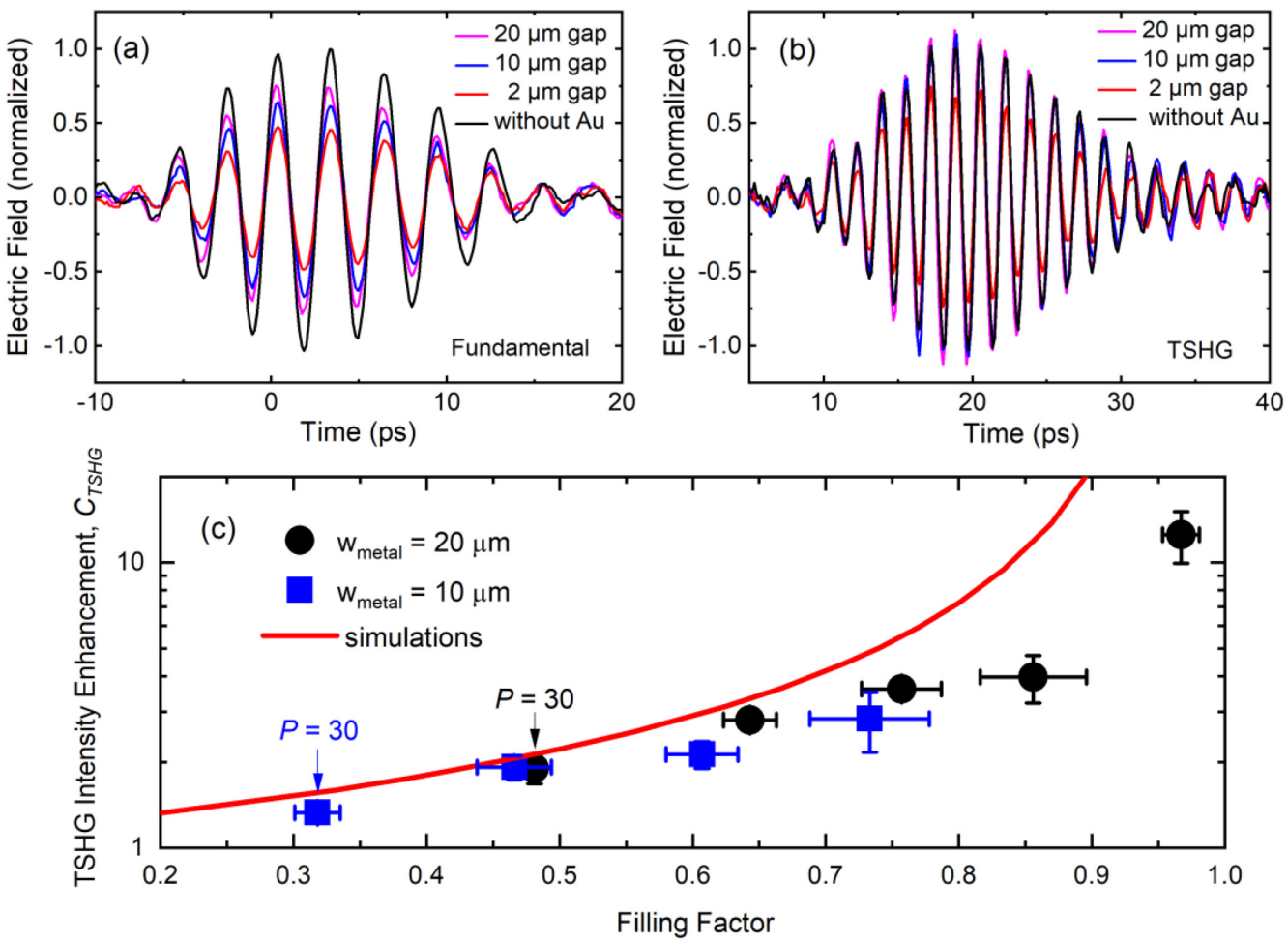

FIG. 3. Comparison of time-domain signals illustrating the impact of the size of the gap between 20 μm-width Au bars in periodic arrays on (a) the transmitted fundamental pulse (E_Ω) with a central frequency of $\Omega = 0.3$ THz and (b) TSHG. (c) Active area TSHG intensity relative enhancement as a function of gold filling factor. The error bars reflect cumulative errors resulting from statistical variations in both the width of the gold bars and the gap sizes within the periodic arrays. The solid red line represents the outcome of the numerical simulations detailed in Sec. V.

the Au metal stripes, which is influenced by the gap size. As the gap size decreases, reflection becomes more pronounced, leading to a reduction in the anticipated TSHG field enhancement capability of the periodic array [see Fig. 7(a) in Sec. V]. Figure 3(b) presents the TSHG amplitude behavior for these hybrid structures. We observe a slight enhancement of the TSHG field at nominal gap sizes of 20 and 10 μm, measured in the far-field geometry; conversely, at 2 μm, the TSHG peak field amplitude diminishes to 70% of the TSHG signal from the bare reference sample. The origin of the increased reflection with the decrease in gap size is attributed to the rearrangement of the THz electric field, E_x, profile between the edges of the Au stripes [see Fig. 7(b) in Sec. V], as indicated by the simulations discussed in Sec. V.

For a more quantitative and accurate description, we apply fast Fourier transforms (FFTs) to the signals in Fig. 3(b) and calculate the integrated intensity for each spectrum, denoted by I_{TSHG}. To account for the TSHG enhancement factor in the gold grating structures, we normalize the detected TSHG intensity to the active area $A_{\mathrm{active}} = 1 - F$ of the periodic arrays. Consequently, the experimental THz field *relative* enhancement factor, G_r, can be expressed as

$$G_r^4 \equiv C_{\mathrm{TSHG}} = I_{\mathrm{TSHG}}^{\mathrm{grating}} / \left(I_{\mathrm{TSHG}}^{\mathrm{no\ grating}} \times A_{\mathrm{active}} \right), \tag{2}$$

where C_{TSHG} is defined as the relative TSHG intensity enhancement factor, representing the enhancement within the gap of the periodic arrays. $I_{\mathrm{TSHG}}^{\mathrm{grating}}$ and $I_{\mathrm{TSHG}}^{\mathrm{no\ grating}}$ denote the TSHG intensity measured from samples with the grating structure and reference bare Py/Pt sample, respectively. The enhancement factor C_{TSHG}, as a function

of the filling factor for samples with varying gap sizes, is summarized in Fig. 3(c). To illustrate experimentally that the enhancement factor scales with the grating filling factor, we plot the data for periodic arrays with two Au stripe widths of $w_{metal} = 20\,\mu$m and of $w_{metal} = 10\,\mu$m. It is evident that the experimental data exhibit a smooth trend as a function of the filling factor, progressively increasing as F approaches unity, supporting a 12-fold increase in the TSHG intensity at a gap size of approximately $1\,\mu$m and a gold width of $20\,\mu$m [at $F = 0.97$ in Fig. 3(c)]. Conversely, samples with identical nominal periods (indicated by arrows of corresponding colors) display different values of C_{TSHG}.

Next, using both, numerical and FEM simulations (see Sec. V), we calculated the relative enhancement of the absorbed fundamental power in the gap due to the grating, considering different filling factors. This relative enhancement is represented by the ratio $\alpha^{grating}/\alpha^{no\ grating}$, where $\alpha^{grating}$ and $\alpha^{no\ grating}$ are the absorption coefficients with and without the grating structure, respectively. Given that the TSHG intensity enhancement factor C_{TSHG} scales quadratically with the fundamental radiation absorption enhancement, we plot the theoretical $C_{TSHG} = (\alpha^{grating}/\alpha^{no\ grating})^2$ against the filling factor in Fig. 3(c) (solid red line). We observe a good correlation between the simulations and experimental data at low filling factors (relatively large gap sizes). However, as the filling factor approaches unity, our calculations predict a stronger enhancement than what is experimentally observed. The origin of this discrepancy at high F will be addressed in Sec. V. Notably, our simulation results already indicate a significant decline in TSHG enhancement potential compared to the ideal limit. For instance, at $F = 0.85$, the ideal second harmonic generation enhancement factor is expected to be $G^4 = \frac{1}{(1-F)^4} \sim 10^3$, whereas our calculations, accounting for enhanced reflection, predict only a factor of 10 [Fig. 3(c)]. These results indicate that to achieve improved TSHG performance using grating structures in far-field geometry, it will be necessary to employ spintronic active interfaces made from materials that are less conductive than conventional metallic FMs and HMs. Nonetheless, for magnetic memory applications and antenna rectifiers, the use of FM/HM nanomagnets is advantageous.[42] In this regard, reflection losses, which appear to be quite parasitic in our samples, may be reduced compared to continuous thin-film systems.

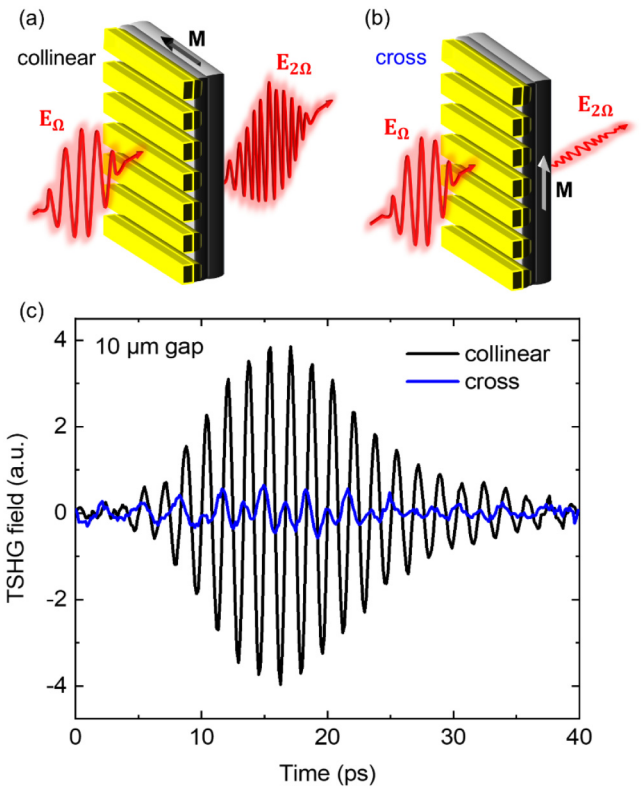

FIG. 4. Comparison of TSHG amplitudes for two distinct in-plane magnetization directions: (a) parallel and (b) perpendicular to the long axis of the Au stripes. (c) In the case where the Py magnetization aligns parallel to the Au stripes' long axis, the TSHG polarization is parallel to the fundamental beam polarization, and the signal is detected in a collinear configuration (black line). Conversely, when the Py magnetization is perpendicular to the Au stripes, the TSHG polarization is detected in a cross-polarization geometry. The reduced TSHG amplitude in the cross-configuration (blue line) is attributed to the enhanced reflection of the TSHG wave from the gold arrays. This reflected wave, which is phase shifted by π, interferes with the forward-propagated TSHG destructively, resulting in a vanishing signal.

IV. MAGNETIZATION CONTROL OF SPINTRONIC TSHG CHARACTERISTICS

A. TSHG valve using grating structures

It has been demonstrated that, analogous to STEs, the polarization plane of spintronic second harmonic generation can be controlled by the orientation of magnetization in the FM layer, as the polarization of the spin current aligns with the magnetization direction.[18] With the transverse spin-to-charge conversion due to the inverse spin Hall effect in the HM layer, the TSHG polarization plane remains orthogonal to the magnetization direction, irrespective of the polarization of the fundamental beam.[18] When integrated with grating structures, this phenomenon enables additional functionality, such as TSHG switching through the manipulation of the Py magnetization. Figure 4 illustrates this TSHG valve behavior in our hybrid heterostructure sample with $w_{metal} = 20\,\mu$m and $w_{gap} = 10\,\mu$m, where the far-field TSHG amplitude remains unchanged [as seen in Fig. 3(b)]. When the Py magnetization (M) is aligned parallel to the direction of the Au stripes [as shown in the schematic of Fig. 4(a)], we observe TSHG with a polarization plane perpendicular to the Au bars, which is collinear with the incident fundamental pulse polarization (E_Ω). In the cross-polarization geometry, when M is oriented perpendicular to the Au bars [as depicted in the schematic of Fig. 4(b)], the TSHG polarization plane aligns with the long axis of the Au stripes. As can be seen in Fig. 4(c), the TSHG amplitude can be switched on (in collinear geometry) and off (in cross-polarization geometry), depending on the magnetization orientation. The reduced TSHG signal in the cross-polarization geometry is attributed to the back-propagating TSHG wave, which has a polarization plane-parallel to the Au bars. This condition leads

to reflection from the grating microstructure, resulting in destructive interference with the forward-propagating TSHG wave.

We note that when detecting the grating-enhanced rectified signal associated with second harmonic generation in the near-field geometry, or even through electrical means, this valve concept facilitates more efficient rapid (on the order of tens of picoseconds) readout of FM magnetization using THz pulses. By controlling the magnetic orientation in conjunction with the grating structure, the properties of the generated THz signal can be effectively switched. This capability supports the development of fast and efficient techniques for reading magnetization states, which is essential for high-speed data processing applications.

B. TSHG cavity using grating structures

We also explore the TSHG cavity resonances[41] by positioning the 20 μm-width gold bars on the side of the quartz glass substrate opposite to the metallic film. To achieve cavity enhancement, constructive interference must occur between the forward- and back-propagating TSHG fields emitted from the Py/Pt interface. This requires that the round-trip time of the back-propagating TSHG beam approximately matches an integer (N) multiple of the TSHG oscillation period, as described by the following equation: $2\ln/c = Nt_{\mathrm{SHG}}$. Here, t_{SHG} is the TSHG field period, c is the speed of light, $l = 1$ mm is the substrate thickness, and $n = 1.95$ is the refractive index of the substrate at THz frequencies.[43] With $2\ln/c = 13$ ps, we calculate a frequency of 0.692 THz for $N = 9$. Therefore, we adjust the THz fundamental radiation frequency to 0.35 THz to establish a TSHG resonant F–P type cavity within the quartz glass substrate.

By applying an external magnetic field, we can control the magnetization of the Py layer to align either perpendicular [cross-configuration, Fig. 5(a)] or parallel [collinear configuration, Fig. 5(b)] to the long axis of the gold stripes, as illustrated in the top panel of Fig. 5. In the cross-configuration geometry, the TSHG polarization plane aligns with the long axis of the gold stripes, facilitating the reflection of the back-propagating TSHG signal and constructive interference with the forward-propagating signal. This configuration yields a TSHG cavity enhancement effect of approximately 50% in amplitude compared to the bare Py/Pt reference sample [Fig. 5(c)]. Additionally, our cavity sample exhibits longer and spectrally narrower TSHG pulses, as shown in Figs. 5(c) and 5(e), respectively. In the collinear configuration, where the Py magnetization is aligned parallel to the gold stripes, the TSHG polarization becomes orthogonal to the long axis of the stripes. As a result, the back-propagating TSHG radiation passes through the periodic arrays without inducing cavity enhancement, which is evident when comparing the signals of this configuration to those of the reference (bare) samples in Fig. 5(d) and their FFT spectra in Fig. 5(f). Note that in the reference sample, the TSHG signal in the collinear configuration is larger than that in the cross-configuration due to an additional contribution to the thermally driven TSHG.[18] This contribution arises from the ultrafast unidirectional spin Hall magnetoresistance effect, as previously reported.[13] Thus, studies on cavity geometry demonstrate the ability to actively manipulate the TSHG pulse envelope and timing by aligning the magnetization in the FM layer relative to the long axis of the stripes. This control enables effective tuning of the TSHG pulse duration and can increase its total energy [Fig. 5(e)] by adjusting the FM magnetization.

V. FEM SIMULATION OF GRATING SAMPLES

A. Simulation details

To complement experimental observations of the hybrid structure with a subwavelength gold grating, we performed simulations using the finite element method (FEM) with the commercial software ANSYS HFSS (2025 R1). The simulation model includes 1 mm of SiO_2 substrate, a 2 nm thick Pt and Py layers, a 10 nm layer of SiO_2, and finally the metallic grating with a thickness of 20 nm. A unit cell with this stack is laterally expanded to infinity by periodic boundary conditions. The unit cell is completed by two Floquet ports located at the distance of 300 μm above and under the substrate with the periodic structure. A set of specular modes, defined on the ports, carry an excitation power and allow for capturing reflected and transmitted power. For simulation of the ultrathin metallic layers of Pt and Py, we use layered impedance boundaries with shell elements.[44] Au grating on top is modeled by finite conductivity boundaries with shell elements. In all these boundaries, DC conductivities of thin metallic layers are used.[45–47] For the SiO_2 layer and the substrate, we use a complex permittivity value $4.4 + 0.0063i$. Additionally, we also performed simulations using rigorous coupled wave analysis (RCWA), as implemented in Ref. 48. RCWA offers high computational efficiency and accuracy for periodic structures, enabling rapid parametric studies, while FEM provides greater flexibility for modeling complex geometries, albeit with increased computational cost.

Using both simulation approaches, we extracted the reflected, transmitted, and absorbed THz radiation intensities, which were then employed to calculate the average TSHG intensity enhancement, C_{TSHG}, within the grating gap, as shown in Fig. 3(c). Since both methods produce nearly identical results, Fig. 3(c) presents the simulation data obtained via RCWA.

B. Simulation results

Figure 6 illustrates the FEM simulated THz frequency dependence of the reflection [Fig. 6(a)], transmission [Fig. 6(b)], and absorption [Fig. 6(c)] power for three experimental systems: an Au grating on a SiO_2 substrate, a metallic Py/Pt film, and an Au grating ($w_{\mathrm{metal}} = 20\,\mu$m and $w_{\mathrm{gap}} = 20\,\mu$m) combined with Py/Pt (hybrid structure). All data exhibit periodic variations with incident THz frequency, which are attributed to F–P resonances within the 1 mm-thick SiO_2 substrate. Notably, at specific frequencies—corresponding to constructive interference of multiple reflections at the substrate interfaces—the Au grating structure demonstrates near-complete THz power transmission with minimal reflection and absorption, consistent with the analytical predictions presented in Ref. 24. Conversely, at frequencies where destructive interference occurs, reflection increases up to 40% [Fig. 6(b)], resulting in a corresponding reduction in transmitted power. Noteworthy, the absorption remains minimal across all frequencies [Fig. 6(c)], not exceeding a value of 0.005. Adding Py/Pt film on top of the substrate introduces frequency-dependent absorption, reaching a maximum at frequencies where multiple reflections in the substrate interfere

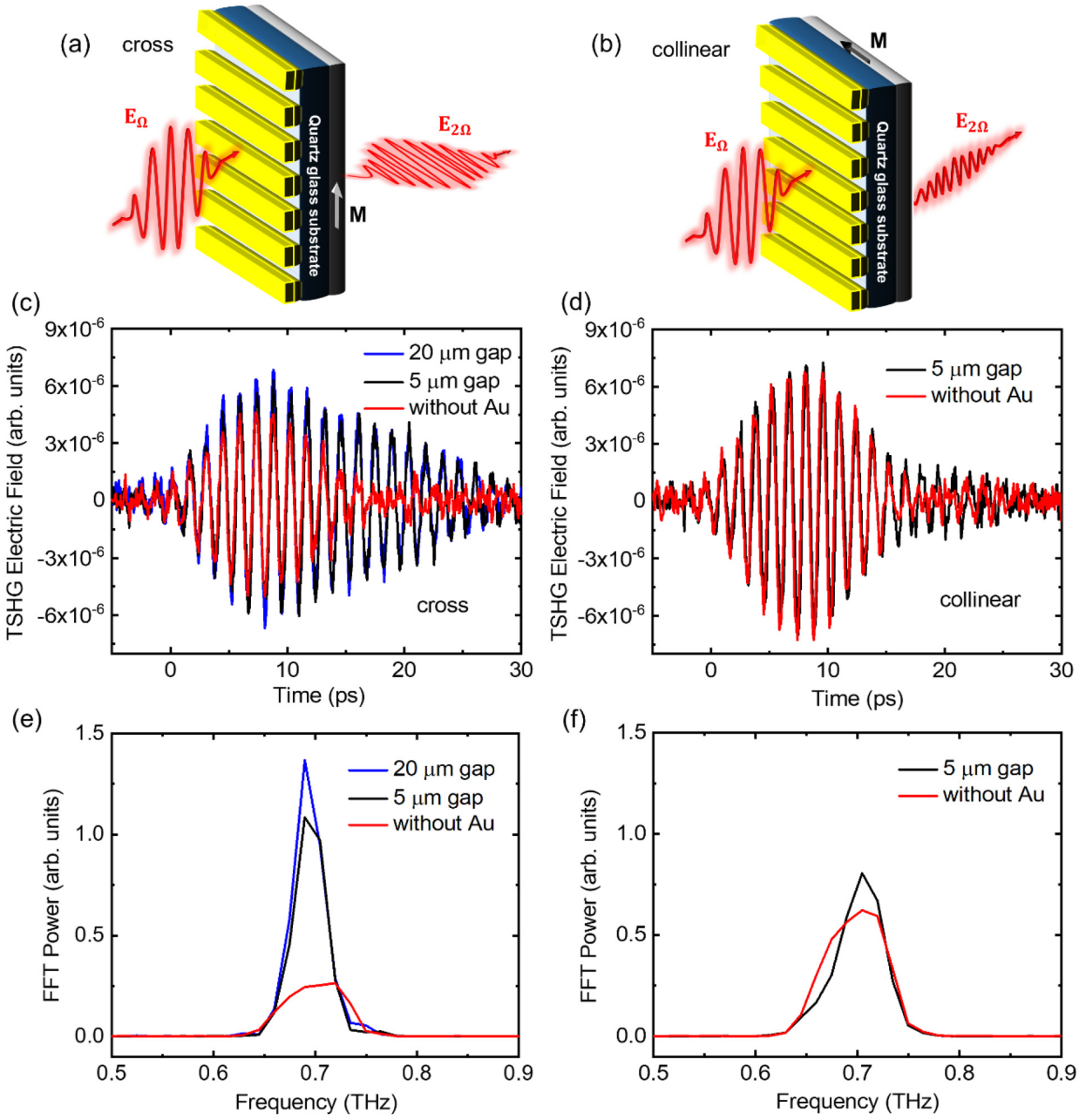

FIG. 5. Cavity-enhanced TSHG using Au stripe arrays on the backside of a quartz glass substrate. The top panel illustrates the Py magnetization alignment for the cross (a) and collinear (b) configurations. (c) Comparison of TSHG signals in the cross-polarization geometry between samples with different gap sizes in the gold periodic arrays and the reference sample without grating structures. (d) presents the same comparison as in (c), but for the collinear polarization geometry. (e) and (f) depict the FFT spectra of the signals from (c) and (d), respectively.

constructively [red curve in Fig. 6(c)]. Combined with Au grating into the hybrid structure, this stack exhibits even further increased reflection and nearby unchanged absorption [black curve in Fig. 6(c)], resulting in comparable TSHG signal amplitudes when measured in the far-field geometry, as shown in Fig. 3(b). Consequently, the TSHG intensity enhancement factor due to the grating structure in this scenario is approximately a factor of two [see Fig. 3(c) for $F \approx 0.5$].

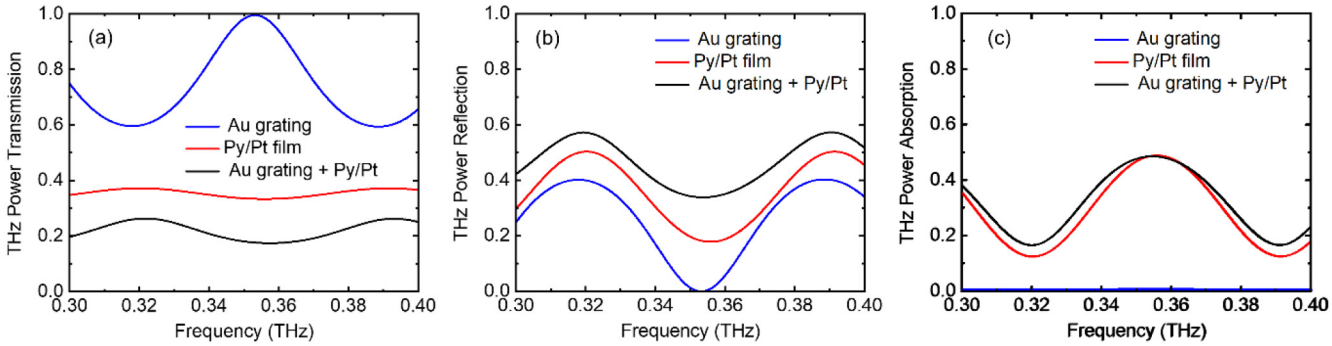

FIG. 6. Comparison of fundamental THz power (a) transmission, (b) reflection, and (c) absorption as a function of radiation frequency for three samples: a gold grating on the substrate (blue line), a bare Py/Pt reference sample (red line), and a gold grating Py/Pt hybrid structure (black line). FEM simulations were conducted for gold gratings with $w_{metal} = 20\,\mu m$ and $w_{gap} = 20\,\mu m$. The data were obtained at the second Floquet port placed $300\,\mu m$ away from the back (nonmetallic) side of the SiO_2 substrate.

Next, we analyze the reduction in THz field transmission with decreasing gap size in our hybrid systems, as observed in Fig. 3(a). Simulations indicate a significant increase in reflection, with the reflected THz power nearly doubling as the grating gap narrows from 20 to $2\,\mu m$ [black curve in Fig. 7(a)]. This increased reflection causes a corresponding decrease in transmission, as seen experimentally in Fig. 3(a), and leads to reduced absorption [red curve in Fig. 7(a)]. Consequently, the diminished absorption results in reduced TSHG efficiency, as visible in Fig. 3(b), along with a much smaller TSHG intensity enhancement than would be expected without the effects of enhanced reflection. This behavior is attributed to changes in the THz electric field component profile between the Au bars, which significantly vary with decreasing gap size. Figure 7(b) presents the normalized electric field distribution, E_x, along the x axis [across the gap, see schematics in Fig. 1(a)] for the Au grating on a substrate (dashed lines) and the hybrid structure (solid lines). The overall reduction in electric field amplitude enhancement within the hybrid structure is evident. For the gold grating on a substrate, the electric field distribution at the Au edges with a $20\,\mu m$ gap is considerably broader compared to the hybrid system, and these broad peaks overlap within the gap when the gap size is reduced to $2\,\mu m$ [red dashed line in Fig. 7(b)]. As already

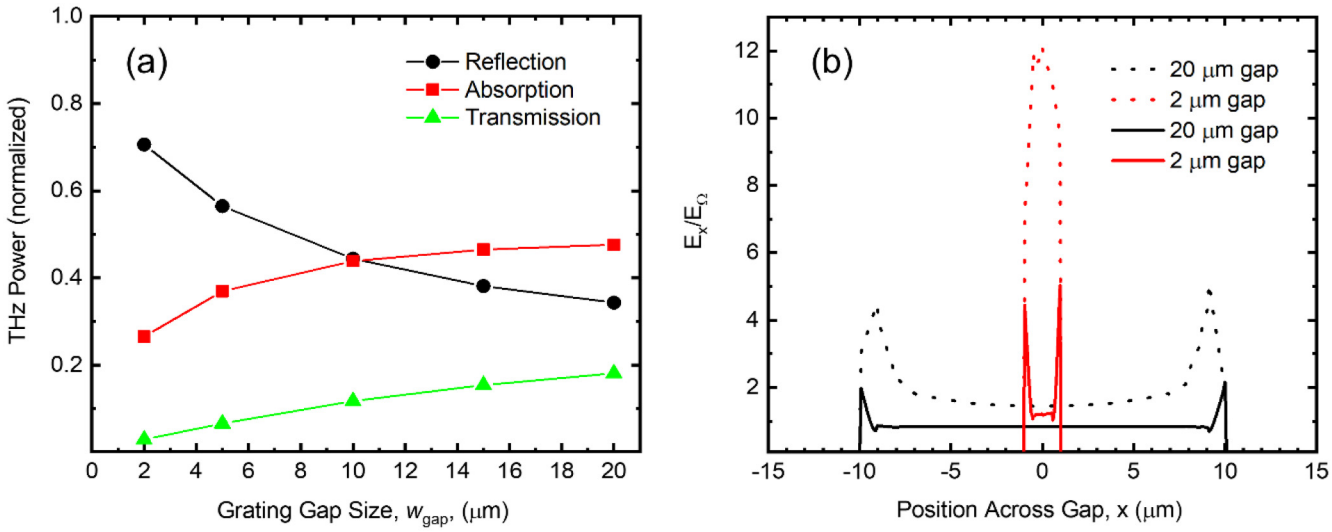

FIG. 7. (a) THz power reflection (black), transmission (green), and absorption (red) as functions of gap width in gold grating Py/Pt hybrid structures. The data show FEM results for gold gratings with $w_{metal} = 20\,\mu m$. (b) Profiles of the THz electric field component, E_x, across the gap, normalized to the incident THz field, E_Ω, for a gold grating on the substrate (dashed lines) and a gold grating Py/Pt hybrid structure (solid lines) with $w_{gap} = 20\,\mu m$ (black) and $w_{gap} = 2\,\mu m$ (red). The center of the gap between the Au bars is denoted as x = 0.

shown in Fig. 2(b), a field enhancement factor of more than ten can be achieved at a 2 μm gap ($F = 0.91$). In the hybrid structure with a 20 μm gap, the electric field distribution across the gap appears nearly uniform, with narrower peaks at the edges of the gold bars [solid black line Fig. 7(b)]. Reducing the gap from 20 to 2 μm increases the electric field only by about a factor of two, accompanied by a significant change in the field profile compared to the distribution in the sample without the Py/Pt layer, demonstrating a clear degradation of the gap-averaged field amplitude in the hybrid system relative to the gold grating on a substrate.

In the experiment, the modification of the THz field profile at smaller gap sizes is not the sole cause of the reduced TSHG efficiency, as evidenced by the discrepancy between simulation data and experimental results at larger filling factors in Fig. 3(c). This mismatch in the relative TSHG enhancement cannot be ascribed to the F–P effect since Py/Pt samples with and without Au grating exhibit similar behavior [Fig. 6(c)], thereby excluding the F–P contribution based on their ratio. A possible impact from imperfections at the edges of the gold stripes, potentially significant at smaller gaps, is also ruled out, as the transmitted fundamental pulse amplitude shown in Fig. 2(a) exhibits negligible dependence on the gap width down to the nominal 2 μm. The remaining factor is the spintronic THz frequency conversion mechanism, which is not accounted for in our simulations. Based on our preliminary simulation results, the effect of ultrafast backflow currents, recently proposed for STEs,[49] does not significantly alter the TSHG efficiency. The estimated cutoff frequencies show little gap dependence in the gold grating structure, contrary to the increasing discrepancy between calculations and experimental data as the gap size decreases [Fig. 3(c)]. What remains is the TSHG saturation effect. Since the spin-to-charge conversion in Pt is unlikely to be a limiting factor at our frequencies, we suggest that the observed saturation results from the saturation of Py demagnetization at THz field amplitudes above 250 kV/cm.

VI. CONCLUSIONS

We examined the impact of gold grating structures on spintronic THz frequency conversion efficiency by varying gap sizes and stripe widths in periodic arrays. Our results show that enhanced reflection from metallic Py/Pt layers, the THz conversion source, limits far-field TSHG amplitude enhancement. However, these hybrid structures yield significant gap-localized TSHG intensity increases, reaching nearly an order of magnitude as the grating filling factor approaches unity—beneficial for near-field spintronic elements such as rapid magnetization readouts. Crucially, the spintronic nature of the conversion mechanism in gold-grated Py/Pt samples enables efficient control of the TSHG signal amplitude by adjusting the Py magnetization orientation relative to the Au stripe axis, thereby enhancing prospects for high-speed memory and data processing through efficient magnetization state readout. Positioning periodic arrays on the quartz substrate's backside induces modest TSHG cavity enhancement in the cross-configuration, with Py magnetization perpendicular to the gold stripes. This cavity design also doubles the pulse duration and the number of cycles, altering the carrier envelope. By aligning the ferromagnetic layer's magnetization, tunable pulse duration and shape are achieved, providing enhanced control over the timing and profile of the TSHG envelope without sacrificing the signal intensity.

ACKNOWLEDGMENTS

Support of the nanofabrication facilities at the Ion Beam Center Rossendorf (NanoFaRo) is gratefully acknowledged. The authors are grateful to Thomas Naumann and Tommy Schönherr for experimental and technical support. Parts of this research were carried out at ELBE at the Helmholtz-Zentrum Dresden-Rossendorf e.V., a member of the Helmholtz Association. R.S. and A.L. acknowledge support from the German Research Foundation (DFG) Grant No. 464974971. K.-J.T. acknowledges funding from the European Union's Horizon 2020 research and innovation program under Grant Agreement No. 101125457 (ERC CoG "EQUATE"). ICN2 is funded by the CERCA Programme/Generalitat de Catalunya and supported by the Severo Ochoa Centers of Excellence program, Grant No. CEX2021-001214-S, funded by MCIN/AEI/10.13039.501100011033.

AUTHOR DECLARATIONS

Conflict of Interest

The authors have no conflicts to disclose.

Author Contributions

Hatice Nur Koyun: Data curation (equal); Formal analysis (equal); Investigation (equal); Methodology (equal); Writing – original draft (equal); Writing – review & editing (equal). **Ruslan Salikhov:** Conceptualization (lead); Data curation (lead); Formal analysis (lead); Investigation (lead); Methodology (equal); Project administration (equal); Supervision (equal); Validation (equal); Visualization (equal); Writing – original draft (lead); Writing – review & editing (lead). **Ciaran Fowley:** Conceptualization (equal); Data curation (equal); Formal analysis (equal); Investigation (equal); Methodology (equal); Resources (equal); Supervision (equal); Validation (equal); Visualization (equal); Writing – original draft (equal); Writing – review & editing (equal). **Steffen Kober:** Data curation (equal); Formal analysis (supporting); Investigation (equal); Methodology (supporting); Validation (supporting); Visualization (supporting); Writing – review & editing (supporting). **Nupur Sontakkey:** Software (equal); Visualization (equal). **Igor Ilyakov:** Conceptualization (supporting); Data curation (supporting); Formal analysis (supporting); Investigation (supporting); Methodology (equal); Validation (supporting); Writing – original draft (equal). **Thales V. A. G. de Oliveira:** Data curation (supporting); Investigation (supporting); Methodology (supporting); Validation (supporting); Writing – original draft (supporting); Writing – review & editing (supporting). **Jan-Christoph Deinert:** Data curation (supporting); Investigation (supporting); Methodology (supporting); Validation (supporting); Writing – original draft (supporting). **Aleksandra Lindner:** Conceptualization (supporting); Funding acquisition (lead); Investigation (supporting); Project administration (equal); Resources (equal); Writing – original draft (supporting). **Artur Erbe:** Conceptualization (supporting); Formal analysis (supporting); Funding acquisition (supporting); Investigation (supporting);

Project administration (equal); Supervision (lead); Writing – original draft (supporting). **Jürgen Faßbender:** Conceptualization (supporting); Formal analysis (supporting); Funding acquisition (lead); Investigation (supporting); Methodology (supporting); Project administration (lead); Resources (supporting); Supervision (supporting); Validation (supporting); Writing – original draft (supporting); Writing – review & editing (supporting). **Manfred Helm:** Conceptualization (supporting); Formal analysis (supporting); Funding acquisition (lead); Investigation (supporting); Methodology (supporting); Project administration (lead); Resources (supporting); Supervision (supporting); Validation (supporting); Writing – original draft (supporting); Writing – review & editing (supporting). **Jürgen Lindner:** Conceptualization (lead); Data curation (supporting); Formal analysis (equal); Funding acquisition (equal); Investigation (equal); Methodology (equal); Project administration (lead); Resources (lead); Software (supporting); Supervision (lead); Validation (equal); Visualization (equal); Writing – original draft (equal); Writing – review & editing (equal). **Stephan Winnerl:** Conceptualization (lead); Data curation (supporting); Formal analysis (equal); Funding acquisition (equal); Investigation (equal); Methodology (equal); Project administration (lead); Resources (equal); Supervision (lead); Validation (equal); Visualization (equal); Writing – original draft (equal); Writing – review & editing (equal). **Klaas-Jan Tielrooij:** Formal analysis (equal); Funding acquisition (lead); Investigation (equal); Methodology (equal); Project administration (lead); Resources (lead); Software (lead); Supervision (lead); Validation (equal); Visualization (lead); Writing – original draft (equal); Writing – review & editing (equal). **Ryszard Narkowicz:** Formal analysis (lead); Investigation (supporting); Methodology (supporting); Software (lead); Validation (lead); Visualization (lead); Writing – review & editing (lead). **Sergey Kovalev:** Conceptualization (lead); Data curation (lead); Formal analysis (equal); Investigation (lead); Methodology (lead); Resources (equal); Supervision (equal); Validation (equal); Visualization (lead); Writing – original draft (equal); Writing – review & editing (equal).

DATA AVAILABILITY

The data that support the findings of this study are available from the corresponding authors upon reasonable request.

REFERENCES

[1]A. Kirilyuk, A. V. Kimel, and T. Rasing, "Ultrafast optical manipulation of magnetic order," Rev. Mod. Phys. **82**, 2731–2784 (2010).

[2]J. Walowski and M. Münzenberg, "Perspective: Ultrafast magnetism and THz spintronics," J. Appl. Phys. **120**, 140901 (2016).

[3]B. Dieny, I. L. Prejbeanu, K. Garello, P. Gambardella, P. Freitas, R. Lehndorff, W. Raberg, U. Ebels, S. O. Demokritov, J. Akerman *et al.*, "Opportunities and challenges for spintronics in the microelectronics industry," Nat. Electron. **3**, 446–459 (2020).

[4]A. Hirohataa, K. Yamadab, Y. Nakatanic, I.-L. Prejbeanud, B. Diény, P. Pirro, and B. Hillebrandse, "Review on spintronics: Principles and device applications," J. Magn. Magn. Mater. **509**, 166711 (2020).

[5]T. Seifert, S. Jaiswal, U. Martens, J. Hannegan, L. Braun, P. Maldonado, F. Freimuth, A. Kronenberg, J. Henrizi, I. Radu *et al.*, "Efficient metallic spintronic emitters of ultrabroadband terahertz radiation," Nat. Photonics **10**, 483 (2016).

[6]Z. Feng, H. Qiu, D. Wang, C. Zhang, S. Sun, B. Jin, and W. Tan, "Spintronic terahertz emitter," J. Appl. Phys. **129**, 010901 (2021).

[7]W. Wu, C. Y. Ameyaw, M. F. Doty, and M. B. Jungfleisch, "Principles of spintronic THz emitters," J. Appl. Phys. **130**, 091101 (2021).

[8]T. S. Seifert, L. Cheng, Z. Wie, T. Kampfrath, and J. Qi, "Spintronic sources of ultrashort terahertz electromagnetic pulses," Appl. Phys. Lett. **120**, 180401 (2022).

[9]R. Rouzegar, A. L. Chekhov, Y. Behovits, B. R. Serrano, M. A. Syskaki, C. H. Lambert, D. Engel, U. Martens, M. Münzenberg, M. Wolf *et al.*, "Broadband spintronic terahertz source with peak electric field exceeding 1.5 MV/cm," Phys. Rev. Appl. **19**, 034018 (2023).

[10]C. Liu, S. Wang, S. Zhang *et al.*, "Active spintronic-metasurface terahertz emitters with tunable chirality," Adv. Photonics **3**, 056002 (2021).

[11]R. Salikhov, I. Ilyakov, L. Körber, L. A. Kákay, R. A. Gallardo, A. Ponomaryov, J.-C. Deinert, T. V. A. G. Oliveira, K. Lenz, J. Fassbender, S. Bonetti, O. Hellwig, J. Lindner, and S. Kovalev, "Coupling of terahertz light with nanometrewavelength magnon modes via spin-orbit torque," Nat. Phys. **19**, 529–535 (2023).

[12]Y. Behovits, A. L. Chekhov, S. Y. Bodnar, O. Gueckstock, S. Reimers, Y. Lytvynenko, Y. Skourski, M. Wolf, T. S. Seifert, O. Gomonay, M. Kläui, M. Jourdan, and T. Kampfrath, "Terahertz Néel spin-orbit torques drive nonlinear magnon dynamics in antiferromagnetic Mn_2Au," Nat. Commun. **14**, 6038 (2023).

[13]R. Salikhov, I. Ilyakov, A. Reinold, J.-C. Deinert, T. de Oliveira, A. Ponomaryov, G. L. Prajapati, P. Pilch, A. Ghalgaoui, M. Koch *et al.*, "Ultrafast unidirectional spin Hall magnetoresistance driven by terahertz light field," Nat. Commun. **16**, 2249 (2025).

[14]R. Salikhov, M. Lysne, P. Werner, I. Ilyakov, M. Schüler, T. V. A. G. de Oliveira, A. Ponomaryov, A. Arshad, G. L. Prajapati, J.-C. Deinert *et al.*, "Spin-orbit interaction driven terahertz nonlinear dynamics in transition metals," npj Spintronics **3**, 3 (2025).

[15]M. Hudl, M. d'Aquino, M. Pancaldi, S.-H. Yang, M. G. Samant, S. S. P. Parkin, H. A. Dürr, C. Serpico, M. C. Hoffmann, and S. Bonetti, "Nonlinear magnetization dynamics driven by strong terahertz fields," Phys. Rev. Lett. **123**, 197204 (2019).

[16]A. L. Chekhov, Y. Behovits, J. J. F. Heitz, C. Denker, D. A. Reiss, M. Wolf, M. Weinelt, P. W. Brouwer, M. Münzenberg, and T. Kampfrath, "Ultrafast demagnetization of iron induced by optical versus terahertz pulses," Phys. Rev. X **11**, 041055 (2021).

[17]C. Pellegrini, S. Sharma, J. K. Dewhurst, and A. Sanna, "*Ab initio* study of ultrafast demagnetization of elementary ferromagnets by terahertz versus optical pulses," Phys. Rev. B **105**, 134425 (2022).

[18]I. Ilyakov, A. Brataas, T. V. A. G. Oliveira, A. Ponomaryov, J.-C. Deinert, O. Hellwig, J. Faßbender, J. Lindner, R. Salikhov, and S. Kovalev, "Efficient ultrafast field-driven spin current generation for spintronic terahertz frequency conversion," Nat. Commun. **14**, 7010 (2023).

[19]R. Rouzegar, L. Brandt, L. Nádvorník, D. A. Reiss, A. L. Chekhov, O. Gueckstock, C. In, M. Wolf, T. S. Seifert, P. W. Brouwer *et al.*, "Laser-induced terahertz spin transport in magnetic nanostructures arises from the same force as ultrafast demagnetization," Phys. Rev. B **106**, 144427 (2022).

[20]J.-H. Kang and Q.-H. Park, "Local enhancement of terahertz waves in structured metals," IEEE Trans. Terahertz Sci. Technol. **6**, 371–381 (2016).

[21]J.-H. Kang, D.-S. Kim, and M. Seo, "Terahertz wave interaction with metallic nanostructures," Nanophotonics **7**, 763–793 (2018).

[22]M. A. Seo, H. R. Park, S. M. Koo *et al.*, "Terahertz field enhancement by a metallic nano slit operating beyond the skin-depth limit," Nat. Photonics **3**, 152–156 (2009).

[23]H. R. Park, Y. M. Park, H. S. Kim, J. S. Kyoung, M. A. Seo, D. J. Park, Y. H. Ahn, K. J. Ahn, and D. S. Kim, "Terahertz nanoresonators: Giant field enhancement and ultrabroadband performance," Appl. Phys. Lett. **96**, 121106 (2010).

[24]A. Novitsky, A. M. Ivinskaya, M. Zalkovskij, R. Malureanu, P. U. Jepsen, and A. Lavrinenko, "Non-resonant terahertz field enhancement in periodically arranged nanoslits," J. Appl. Phys. **112**, 074318 (2012).

[25]A. R. Davoyan, V. V. Popov, and S. A. Nikitov, "Tailoring terahertz near-field enhancement via two-dimensional plasmons," Phys. Rev. Lett. **108**, 127401 (2012).
[26]X. Lu, R. Wan, G. Wang, T. Zhang, and W. Zhang, "Giant and tunable electric field enhancement in the terahertz regime," Opt. Express **22**, 27001 (2014).
[27]W. Jia, M. Lou, P. Gopalan, A. Bhattacharyya, S. Krishnamoorthy, and B. Sensale-Rodriguez, "On the terahertz response of metal-gratings on anisotropic dielectric substrates and its prospective application for anisotropic refractive index characterization," J. Appl. Phys. **131**, 193101 (2022).
[28]Y. Mukai, H. Hirori, T. Yamamoto, H. Kageyama, and K. Tanaka, "Nonlinear magnetization dynamics of antiferromagnetic spin resonance induced by intense terahertz magnetic field," New J. Phys. **18**, 013045 (2016).
[29]S. Schlauderer, C. Lange, S. Baierl, T. Ebnet, C. P. Schmid, D. C. Valovcin, A. K. Zvezdin, A. V. Kimel, R. V. Mikhaylovskiy, and R. Huber, "Temporal and spectral fingerprints of ultrafast all-coherent spin switching," Nature **569**, 383–387 (2019).
[30]U. Nandi, M. S. Abdelaziz, S. Jaiswal, G. Jakob, O. Gueckstock, S. M. Rouzegar, T. S. Seifert, M. Kläui, T. Kampfrath, and S. Preu, "Antenna-coupled spintronic terahertz emitters driven by a 1550 nm femtosecond laser oscillator," Appl. Phys. Lett. **115**, 022405 (2019).
[31]F.-F. Stiewe, T. Winkel, Y. Sasaki, T. Tubandt, T. Kleinke, C. Denker, U. Martens, N. Meyer, T. S. Parvini, S. Mizukami *et al.*, "Spintronic emitters for super-resolution in THz-spectral imaging," Appl. Phys. Lett. **120**, 032406 (2022).
[32]C. Rathje, R. von Seggern, L. A. Gräper, J. Walowski, M. Münzenberg, and S. Schäfer, "Coupling broadband terahertz dipoles to microscale resonators," ACS Photonics **10**, 3467–3475 (2023).
[33]Z. Zhang, F. Sekiguchi, T. Moriyama, S. C. Furuya, M. Sato, T. Satoh, Y. Mukai, K. Tanaka, T. Yamamoto, H. Kageyama *et al.*, "Generation of third-harmonic spin oscillation from strong spin precession induced by terahertz magnetic near fields," Nat. Commun. **14**, 1795 (2023).
[34]K. Maruyama, Z. Zhang, M. Takumi, T. Satoh, M. Nakajima, Y. Kanemitsu, and H. Hirori, "Tesla-class single-cycle terahertz magnetic field pulses generated with a spiral-shaped metal microstructure," Appl. Phys. Express **17**, 022004 (2024).
[35]Y. Tao, W. Bingjie, W. Xu, W. Xu, W. Xuejiao, X. Wang, Y. Ren, Z. Xin, K. He, X. Ma *et al.*, "Ionic terahertz metasurface in ultrathin-layered conductive hydrogel by ultrafast laser tailoring," Opt. Laser Technol. **170**, 110252 (2024).
[36]C. Wang, Y. Wen, Y. Tan, S. Zhao, K. Yu, J. Sun, and J. Zhou, "On-demand generation and control of giant terahertz nonlinearity with metasurfaces," Laser Photonics Rev. **19**, 2401224 (2025).
[37]M. Pancaldi, P. Vavassori, and S. Bonetti, "Terahertz metamaterials for light-driven magnetism," Nanophotonics **13**, 1891–1898 (2024).
[38]J.-C. Deinert, D. Alcaraz Iranzo, R. Pérez, X. Jia, H. A. Hafez, I. Ilyakov, N. Awari, M. Chen, M. Bawatna, A. N. Ponomaryov *et al.*, "Grating-graphene metamaterial as a platform for terahertz nonlinear photonics," ACS Nano **15**, 1145 (2021).
[39]K.-J. Tielrooij, A. Principi, D. S. Reig, A. Block, S. Varghese, S. Schreyeck, K. Brunner, G. Karczewski, I. Ilyakov, O. Ponomaryov *et al.*, "Milliwatt terahertz harmonic generation from topological insulator metamaterials," Light Sci. Appl. **11**, 315 (2022).
[40]A. Di Gaspare, C. Song, C. Schiattarella, L. H. Li, M. Salih, A. G. Davies, E. H. Linfield, J. Zhang, O. Balci, A. C. Ferrari *et al.*, "Compact terahertz harmonic generation in the Reststrahlen band using a graphene-embedded metallic split ring resonator array," Nat. Commun. **15**, 2312 (2024).
[41]M. Mičica, A. Wright, P. Koleják, G. Lezier, K. Postava, J. Hawecker, A. De Vetter, J. Tignon, J. Mangeney, H. Jaffres *et al.*, "Spintronic terahertz emitters with integrated metallic terahertz cavities," Nanophotonics **13**, 1899–1907 (2024).
[42]R. Fabiha, M. Suche, E. Topsakal, and S. Bandyopadhyay, "An unconventional ultra-sub-wavelength receiving nano-antenna activated by ac spin pumping and the ac inverse spin Hall effect," arXiv:2502.07162 (2025).
[43]N. Chudpooti, N. Duangrit, A. D. Burnett, J. R. Freeman, T. B. Gill, C. Phongcharoenpanich, U. Imberg, D. Torrungrueng, P. Akkaraekthalin, I. D. Robertson *et al.*, "Wideband dielectric properties of silicon and glass substrates for terahertz integrated circuits and microsystems," Mater. Res. Express **8**, 056201 (2021).
[44]I. Bardi, G. Peng, and L. E. R. Petersson, "Modeling periodic layered structures by shell elements using the finite-element method," IEEE Trans. Magn. **52**, 7402004 (2016).
[45]M. Yamamoto, T. Matsumae, Y. Kurashima, H. Takagi, T. Suga, T. Itoh, and E. Higurashi, "Growth behavior of Au films on SiO_2 film and direct transfer for smoothing Au surfaces," Int. J. Autom. Technol. **13**, 254–260 (2019).
[46]M.-H. Nguyen, D. C Ralph, and R. A Buhrman, "Spin torque study of the spin Hall conductivity and spin diffusion length in platinum thin films with varying resistivity," Phys. Rev. Lett. **116**, 126601 (2016).
[47]N. García, C. Hao, L. Yonghua, M. Muñoz, Y. Chen, Z. Cui, Z. Lu, Y. Zhou, G. Pan, and A. A. Pasa, "Magnetoresistance in thin permalloy film (10 nm thick and 30–200 nm wide) nanocontacts fabricated by e-beam lithography," Appl. Phys. Lett. **89**, 083112 (2006).
[48]S. Zanotto and A. Tredicucci, "Universal lineshapes at the crossover between weak and strong critical coupling in Fano-resonant coupled oscillators," Sci. Rep. **6**, 24592 (2016).
[49]G. Schmidt, B. Das-Mohapatra, and E. T. Papaioannou, "Charge dynamics in spintronic terahertz emitters," Phys. Rev. Appl. **19**, L041001 (2023).